



Numerical study of Alfvén eigenmodes in the Experimental Advanced Superconducting Tokamak

Youjun Hu, Guoqiang Li, N. N. Gorelenkov, Huishan Cai, Wenjun Yang, Deng Zhou, and Qilong Ren

Citation: *Physics of Plasmas* (1994-present) **21**, 052510 (2014); doi: 10.1063/1.4879826

View online: <http://dx.doi.org/10.1063/1.4879826>

View Table of Contents: <http://scitation.aip.org/content/aip/journal/pop/21/5?ver=pdfcov>

Published by the [AIP Publishing](#)

Articles you may be interested in

[Numerical study of compressibility effects on the reversed shear Alfvén eigenmode in tokamak plasma](#)

Phys. Plasmas **20**, 082509 (2013); 10.1063/1.4817962

[Gyrokinetic simulations of reverse shear Alfvén eigenmodes in DIII-D plasmas](#)

Phys. Plasmas **20**, 012109 (2013); 10.1063/1.4775776

[Nonlinear simulation of toroidal Alfvén eigenmode with source and sink](#)

Phys. Plasmas **17**, 042309 (2010); 10.1063/1.3394702

[Kinetic damping of Alfvén eigenmodes in general tokamak geometry](#)

Phys. Plasmas **16**, 072505 (2009); 10.1063/1.3190158

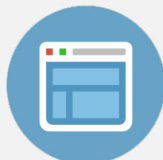
[Kinetic properties of shear Alfvén eigenmodes in tokamak plasmas](#)

Phys. Plasmas **12**, 122501 (2005); 10.1063/1.2135284



Re-register for Table of Content Alerts

Create a profile.



Sign up today!



Numerical study of Alfvén eigenmodes in the Experimental Advanced Superconducting Tokamak

Youjun Hu,^{1,2,a)} Guoqiang Li,¹ N. N. Gorelenkov,³ Huishan Cai,⁴ Wenjun Yang,¹ Deng Zhou,¹ and Qilong Ren¹

¹*Institute of Plasma Physics, Chinese Academy of Sciences, Hefei, Anhui 230031, China*

²*Center for Magnetic Fusion Theory, Chinese Academy of Sciences, Hefei, Anhui 230031, China*

³*Princeton Plasma Physics Laboratory, Princeton, New Jersey 08543-0451, USA*

⁴*Department of Modern Physics, University of Science and Technology of China, Hefei 230026, China*

(Received 10 March 2014; accepted 12 May 2014; published online 29 May 2014)

Alfvén eigenmodes in up-down asymmetric tokamak equilibria are studied by a new magnetohydrodynamic eigenvalue code. The code is verified with the NOVA code for the Solovév equilibrium and then is used to study Alfvén eigenmodes in a up-down asymmetric equilibrium of the Experimental Advanced Superconducting Tokamak. The frequency and mode structure of toroidicity-induced Alfvén eigenmodes are calculated. It is demonstrated numerically that up-down asymmetry induces phase variation in the eigenfunction across the major radius on the midplane. © 2014 AIP Publishing LLC. [<http://dx.doi.org/10.1063/1.4879826>]

I. INTRODUCTION

Alfvén eigenmodes (AEs) can be excited in tokamak plasmas by energetic particles from various sources such as neutral beam injection (NBI), RF heating, and fusion reactions.^{1–7} The AEs can in turn influence the transport of energetic particles and thus are important in determining the performance of NBI/RF heating and future burning plasmas.^{8–12}

Alfvén eigenmodes in tokamak plasmas have been investigated theoretically and experimentally for more than two decades.^{6,7,13–16} Most of the linear properties of AEs are well understood and the methods of identifying AEs in experiments are well developed.^{2,17–19} The studies of AEs in the Experimental Advanced Superconducting Tokamak (EAST) have begun from the experiments in the year 2012.^{20,21} The studies at present focus on identifying the modes and the associated driving sources. The modes observed so far are identified as beta-induced Alfvén eigenmodes (BAEs).²⁰ No obvious toroidicity-induced Alfvén eigenmodes (TAEs) or ellipticity-induced Alfvén eigenmodes (EAEs) have been observed. Recently one NBI line has been installed on EAST and the next campaign of experiments with NBI heating is planned in July of 2014. It is expected that, with the NBI generating energetic particles, various AEs will be routinely observed in the EAST plasmas.

As the first step to understand AEs in the NBI heating EAST plasmas, we need to calculate the frequency and mode structure of AEs for typical EAST parameters. Kinetic theory is often needed in determining the frequency, mode structure, and the stability of AEs.^{22–28} Kinetic effects of fast ions can change the frequency and mode structure of AEs away from those predicted by the ideal magnetohydrodynamic (MHD) theory.^{23,26} However, to a first approximation, the MHD theory can be used to estimate the frequency and mode structure of AEs.^{17,29,30} Various properties of AEs have been studied analytically by the MHD theory.^{17,31,32} Analytical theory of AEs are usually limited to simple equilibria with large aspect-ratio and circular flux surfaces.^{17,31,33} To investigate

AEs in general tokamak equilibria (e.g., equilibria with elongation, triangularity, and up-down asymmetry), numerical codes are usually needed.^{34–39} One of the extensively used AEs codes, the NOVA code,³⁴ solves the ideal MHD eigenmodes equations in general tokamak geometry. However, NOVA along with its kinetic extension NOVA-K^{40,41} is restricted to up-down symmetric equilibria. The equilibria of the EAST discharges are usually up-down asymmetric. To study AEs in this kind of equilibria, we have built a new MHD eigenvalue code named GTAW (General Tokamak Alfvén Waves) which can treat up-down asymmetric equilibria.

For up-down symmetric equilibria, the ideal MHD theory predicts that eigenfunctions have a constant phase (or a phase jump of π) across the major radius on the midplane. However, measurements from the electron cyclotron emission radiometer show that the phase of AEs changes across the radius.^{18,42,43} The change can be due to various effects, including kinetic and geometric effects. In this paper, as an application of the GTAW code, we calculate the frequency and mode structure of TAEs in a up-down asymmetric EAST equilibrium and demonstrate that up-down asymmetry induces radial phase variation in the eigenfunction. In addition, we found that TAEs with frequency near the lower tip of the continuum gap exist in the equilibrium considered, whereas TAEs with frequency near the upper tip of the gap do not exist.

The remainder of this paper is organized as follows. Section II reviews the eigenmodes equations solved in both the NOVA and GTAW codes. The benchmark of GTAW is presented in Sec. III. In Sec. IV, GTAW is applied to the up-down asymmetric EAST equilibrium to calculate the frequency and mode structure of TAEs. A brief summary is given in Sec. V. Appendixes A–D give some formulas used in GTAW.

II. EIGENMODES EQUATIONS IN GENERAL TOKAMAK GEOMETRY

We use the ideal MHD model and assume there is no equilibrium flow. Consider single frequency perturbation of the form $e^{-i\omega t}$, then the linearized ideal MHD equations are written as

^{a)}E-mail: yjhu@ipp.cas.cn

$$-\omega^2 \rho_0 \xi = -\nabla p_1 + \mu_0^{-1} (\nabla \times \mathbf{B}_1) \times \mathbf{B}_0 + \mu_0^{-1} (\nabla \times \mathbf{B}_0) \times \mathbf{B}_1, \quad (1)$$

$$\mathbf{B}_1 = \nabla \times (\xi \times \mathbf{B}_0), \quad (2)$$

and

$$p_1 = -\xi \cdot \nabla p_0 - \gamma p_0 \nabla \cdot \xi, \quad (3)$$

where ξ is the plasma displacement vector, which is related to the perturbed fluid velocity \mathbf{u}_1 by $\mathbf{u}_1 = -i\omega\xi$, \mathbf{B}_1 and p_1 are the perturbed magnetic field and thermal pressure, respectively; \mathbf{B}_0 , p_0 , and ρ_0 are the equilibrium magnetic field, thermal pressure, and mass density, respectively; μ_0 is the vacuum permeability and $\gamma = 5/3$ is the ratio of specific heats. Equations (1)–(3) constitute a closed system for ξ , \mathbf{B}_1 , and p_1 . In order to obtain the component equations of Eqs. (1) and (2) in general tokamak geometry, following Ref. 34, we decompose ξ and \mathbf{B}_1 into components lying in the magnetic surface and perpendicular to it:

$$\xi = \xi_\psi \frac{\nabla \Psi}{|\nabla \Psi|^2} + \xi_s \frac{(\mathbf{B}_0 \times \nabla \Psi)}{B_0^2} + \xi_b \frac{\mathbf{B}_0}{B_0^2}, \quad (4)$$

$$\mathbf{B}_1 = Q_\psi \frac{\nabla \Psi}{|\nabla \Psi|^2} + Q_s \frac{(\mathbf{B}_0 \times \nabla \Psi)}{|\nabla \Psi|^2} + Q_b \frac{\mathbf{B}_0}{B_0^2}, \quad (5)$$

where $\Psi = \Psi_{\text{pol}}/(2\pi) + C$ with C being a constant and Ψ_{pol} being the poloidal magnetic flux within a magnetic surface, ξ_ψ , ξ_s , and ξ_b are the radial, poloidal, and parallel (to \mathbf{B}_0) plasma displacement, respectively, Q_ψ , Q_s , and Q_b are the radial, poloidal, and parallel perturbed magnetic field, respectively. Using Eqs. (4) and (5) in Eqs. (1)–(3), we can obtain the component equations for ξ_ψ , ξ_s , ξ_b , Q_ψ , Q_s , Q_b , and p_1 . Following Ref. 34, we express the final equations in terms of the following four variables: P_1 , ξ_ψ , ξ_s , and $\nabla \cdot \xi$, where $P_1 \equiv p_1 + \mathbf{B}_1 \cdot \mathbf{B}_0/\mu_0$ is the sum of the perturbed thermal and magnetic pressure. Then, the eigenmodes equations can be written in the following matrix form:³⁴

$$\nabla \Psi \cdot \nabla \begin{pmatrix} P_1 \\ \xi_\psi \end{pmatrix} = \begin{pmatrix} C_{11} & C_{12} \\ C_{21} & C_{22} \end{pmatrix} \begin{pmatrix} P_1 \\ \xi_\psi \end{pmatrix} + \begin{pmatrix} D_{11} & D_{12} \\ D_{21} & D_{22} \end{pmatrix} \begin{pmatrix} \xi_s \\ \nabla \cdot \xi \end{pmatrix} \quad (6)$$

and

$$\begin{pmatrix} E_{11} & E_{12} \\ E_{21} & E_{22} \end{pmatrix} \begin{pmatrix} \xi_s \\ \nabla \cdot \xi \end{pmatrix} = \begin{pmatrix} F_{11} & F_{12} \\ F_{21} & F_{22} \end{pmatrix} \begin{pmatrix} P_1 \\ \xi_\psi \end{pmatrix}, \quad (7)$$

where the matrix elements are spatial differential operators on a flux surface. For example, C_{11} , D_{11} , and D_{21} are given, respectively, by

$$C_{11} = 2\kappa_\psi, \quad (8)$$

$$D_{11} = \left(\mu_0^{-1} |\nabla \Psi|^2 S - B_0^2 \sigma \right) \frac{|\nabla \Psi|^2}{B_0^2} \mathbf{B}_0 \cdot \nabla, \quad (9)$$

$$D_{21} = -|\nabla \Psi|^2 \frac{(\mathbf{B}_0 \times \nabla \Psi)}{B_0^2} \cdot \nabla + 2|\nabla \Psi|^2 \kappa_s. \quad (10)$$

The expression for the other matrix elements are given in Appendix A. In Eqs. (8)–(10), $\kappa_\psi \equiv \boldsymbol{\kappa} \cdot \nabla \Psi$ is the normal magnetic curvature with $\boldsymbol{\kappa} \equiv \mathbf{b} \cdot \nabla \mathbf{b}$ being the magnetic curvature vector and $\mathbf{b} \equiv \mathbf{B}_0/B_0$ being the unit vector of the equilibrium magnetic field, $\kappa_s \equiv \boldsymbol{\kappa} \cdot (\mathbf{B}_0 \times \nabla \Psi)/B_0^2$ is the geodesic curvature, $\sigma \equiv \mathbf{B}_0 \cdot \mathbf{J}_0/B_0^2$ with \mathbf{J}_0 being the equilibrium current, and

$$S \equiv \left(\nabla \times \frac{\mathbf{B}_0 \times \nabla \Psi}{|\nabla \Psi|^2} \right) \cdot \frac{(\mathbf{B}_0 \times \nabla \Psi)}{|\nabla \Psi|^2}, \quad (11)$$

is the local magnetic shear.

III. BENCHMARK OF THE GTAW CODE

The GTAW code was developed to solve the eigenmodes Eqs. (6) and (7), which are also the equations solved in the NOVA code.³⁴ The difference between GTAW and NOVA is that NOVA is restricted to up-down symmetric equilibrium while GTAW can deal with up-down asymmetric one. GTAW calculates perturbations with a single toroidal mode number n and thus, the radial plasma displacement ξ_ψ is generally written as

$$\xi_\psi(\psi, \theta, \zeta) = \sum_{m=-\infty}^{\infty} \xi_{\psi m}(\psi) e^{i(m\theta - n\zeta)}, \quad (12)$$

where m is the poloidal mode number, $\xi_{\psi m}(\psi)$ is the amplitude of the poloidal harmonics, (ψ, θ, ζ) is a flux coordinate system with ψ , θ , and ζ being the radial, poloidal, and toroidal coordinate, respectively. The details of the flux coordinate system (ψ, θ, ζ) used in GTAW are given in Appendix B. One thing to note is that location of $\theta=0$ is chosen on the low-field side of the midplane.

To verify GTAW, we use it to calculate the continuum spectra and Alfvén gap modes in a up-down symmetric Solovév equilibrium and compare the results with those given by NOVA. The Solovév equilibrium used in the benchmark case is given by

$$\Psi = \frac{B_0}{2R_0^2 \kappa_0 q_0} \left[R^2 Z^2 + \frac{\kappa_0^2}{4} (R^2 - R_0^2)^2 \right], \quad (13)$$

$$p_0 = p_{0a} - \frac{B_0(\kappa_0^2 + 1)}{\mu_0 R_0^2 \kappa_0 q_0} \Psi, \quad g = g_0, \quad (14)$$

with $B_0 = 1.0$ T, $R_0 = 1.0$ m, $g_0 = 1.0$ mT, $\kappa_0 = 1.5$, $q_0 = 3.0$, and $p_{0a} = 1.1751 \times 10^4$ Pa, where p_0 is the thermal pressure and $g = RB_\phi$ is the toroidal field function of the Grad-Shafranov equation. The flux surface with the minor radius being 0.3 m (corresponding to $\Psi = 2.04 \times 10^{-2} \text{Tm}^2$) is chosen as the boundary flux surface. The flux surfaces and profile of the safety factor q of the equilibrium are plotted in Fig. 1. The plasma is taken to be Deuterium and the number density is taken to be uniform with $n_D = 2 \times 10^{19} \text{m}^{-3}$. Figure 2 compares the $n = 1$ Alfvén continua calculated by

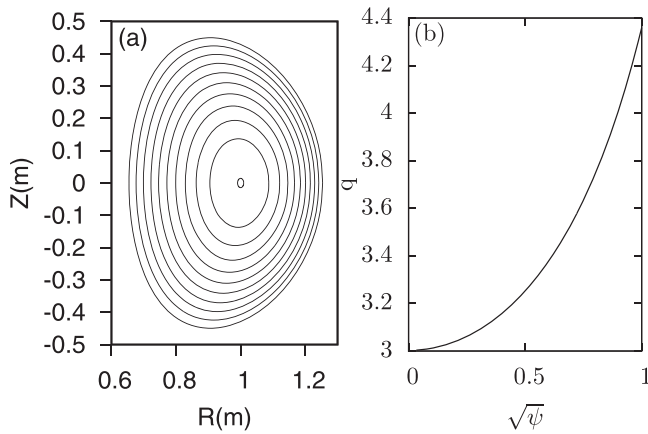


FIG. 1. The flux surfaces (a) and safety factor profile (b) of the Solovév equilibrium used in the benchmark case.

NOVA and GTAW, which shows good agreement between them.

An $n=1$ Alfvén gap mode with frequency $f=297$ kHz is found by both NOVA and GTAW. The mode is identified as a noncircularity-induced Alfvén eigenmode (NAE) because its frequency lies in the NAE gap of the Alfvén continua, as is shown in Fig. 3.

The eigenfunctions of the NAE given by GTAW show that the poloidal harmonics with $m=2$ and $m=5$ are dominant, which is consistent with the expectation that a NAE is formed due to the coupling between m and $m+3$ harmonics. Before comparing the eigenfunctions given by the two codes, we note, as is mentioned above, NOVA is restricted to up-down symmetric equilibrium and, for this case, it can be shown that the amplitude of all the radial displacement harmonics can be transformed to real functions. For this reason, NOVA uses directly real functions for the radial displacement in its calculation. In GTAW, the amplitude of the poloidal harmonics of the radial displacement are complex-valued functions. The Solovév equilibrium used here is up-down symmetric and the results given by GTAW indicate the poloidal harmonics of the radial displacement can be transformed (by multiplying a constant complex number) to real functions. After transforming the radial displacements to real functions, the results can be compared with those of NOVA. Figure 4 compares the radial structure of the

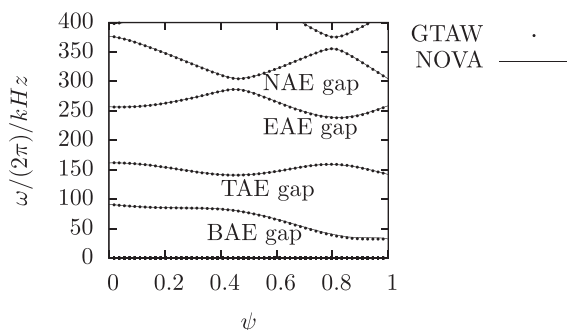


FIG. 2. Comparison of the $n=1$ Alfvén continua calculated by NOVA and GTAW. The continua are calculated in the slow sound approximation⁴⁴ and the equilibrium used is the Solovév equilibrium given in Eqs. (13) and (14).

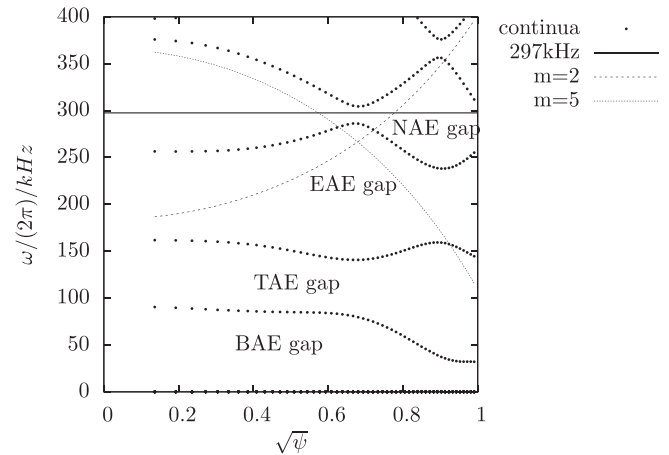


FIG. 3. The frequency $f=297$ kHz is within the NAE gap of the Alfvén continua of the Solovév equilibrium. Also plotted are the $m=2$ and $m=5$ Alfvén continua in the cylindrical limit.

dominant poloidal harmonics ($m=2, 3, 4, 5$) given by the two codes, which also shows good agreement between the two codes.

IV. TAEs IN EAST DISCHARGE #38300

In this section, as an application of the GTAW code, we calculate the frequency and mode structure of TAEs in a up-down asymmetric equilibrium of EAST tokamak. The EAST equilibrium used here was reconstructed by the EFIT code⁴⁵ by using the constraints from experimental diagnostics in EAST discharge #38300 at 3.9 s.⁴⁶ Figure 5 plots the flux surfaces of the equilibrium and the flux coordinates grids within the last closed flux surface (LCFS) used in the numerical calculation. The equilibrium is a double-null configuration with the LCFS connected with the lower X point. The up-down asymmetry can be seen from the shape of the LCFS (besides the shape of flux surfaces, the up-down asymmetry also refers to the distribution of some quantities, e.g., κ_ψ , on a flux surface).

The profiles of the safety factor q , thermal pressure p_0 , and electron number density n_e are plotted in Fig. 6, where it can be seen that p_0 and n_{e0} have transport barriers near the boundary. The electron number density n_{e0} is used here to

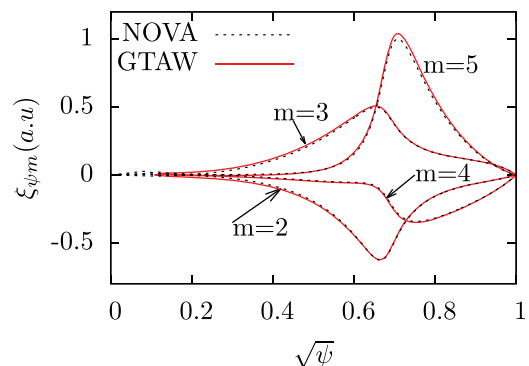


FIG. 4. The dominant poloidal harmonics ($m=2, 3, 4, 5$) of the radial displacement of an $n=1$ NAE as a function of the radial coordinate. The frequency of the mode is $f=297$ kHz. The equilibrium is given by Eqs. (13) and (14).

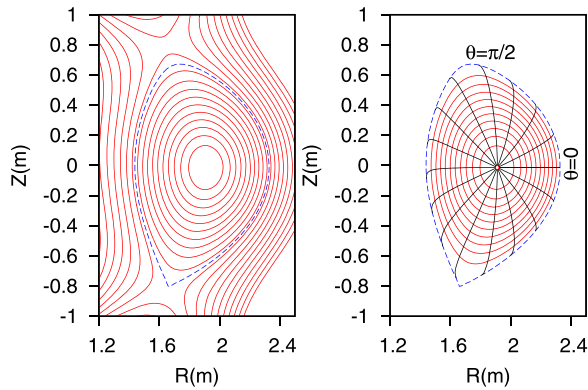


FIG. 5. (a) Flux surfaces of the equilibrium of EAST discharge #38300 at 3.9 s; (b) Flux coordinates grids within the LCFS corresponding to uniform poloidal flux and uniform poloidal arc length (the grids actually used in the numerical calculation are much finer than those plotted in the figure). The coordinate lines corresponding to $\theta = 0$ and $\theta = \pi/2$ are labeled in (b), where θ is the poloidal angle. The dashed lines in (a) and (b) indicate the LCFS, which has $Z_{\max} = 0.67$ m and $Z_{\min} = -0.80$ m. The location of the magnetic axis is at $(R = 1.91$ m, $Z = -1.35 \times 10^{-2}$ m).

determine the plasma mass density through the approximate relation $\rho_0 \approx n_{e0} m_D$, where m_D is the mass of Deuterium ion.

The continua spectra of the equilibrium are plotted in Fig. 7, where two approximations of the full continua are also presented, namely, the zero- β and slow sound approximations,^{23,44} where β is the ratio of the thermal to magnetic pressure. The full ideal MHD continua includes the coupling between Alfvén and sound continua while the zero- β approximation (corresponding to $\gamma = 0$) removes the sound waves from the continua, giving the Alfvén branch of the continua without the thermal pressure contribution. The slow sound approximation also removes the sound branch of the continua but partially retaining the thermal pressure contribution

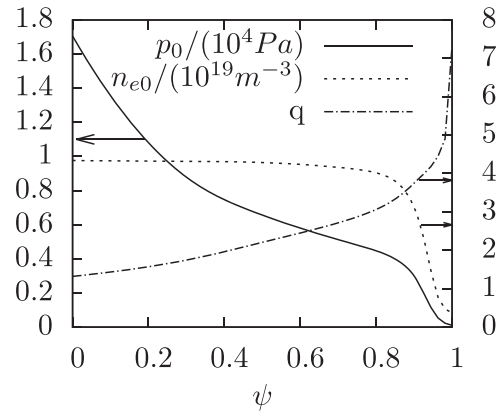


FIG. 6. The radial profiles of the pressure, electron number density, and safety factor for EAST discharge #38300 at 3.9 s.

to the Alfvén branch. The obvious difference between the slow sound and zero- β approximations is that the former has additional frequency gaps (BAE gaps) below the TAE gaps while the latter does not. The continua provide useful information for the experimental observation of AEs, namely, the approximate frequency and radial location of possible AEs. In Fig. 7(c), there are three obvious TAE gaps, which are formed due to the coupling of m and $m + 1$ harmonics with $m = 1, 2, 3$, respectively. In each of the gaps, there can be several AEs with their frequencies within the gap and their radial structures peaking near the gap center. With the toroidal mode number n increasing, the number of TAE gaps usually increases. For instance, Fig. 8 plots the $n = 4$ Alfvén continua, where it can be seen that there are more than eight TAE gaps.

We used GTAW to search modes in the frequency range of the $n = 1$ TAE gaps. A mode with frequency $f = 103$ kHz

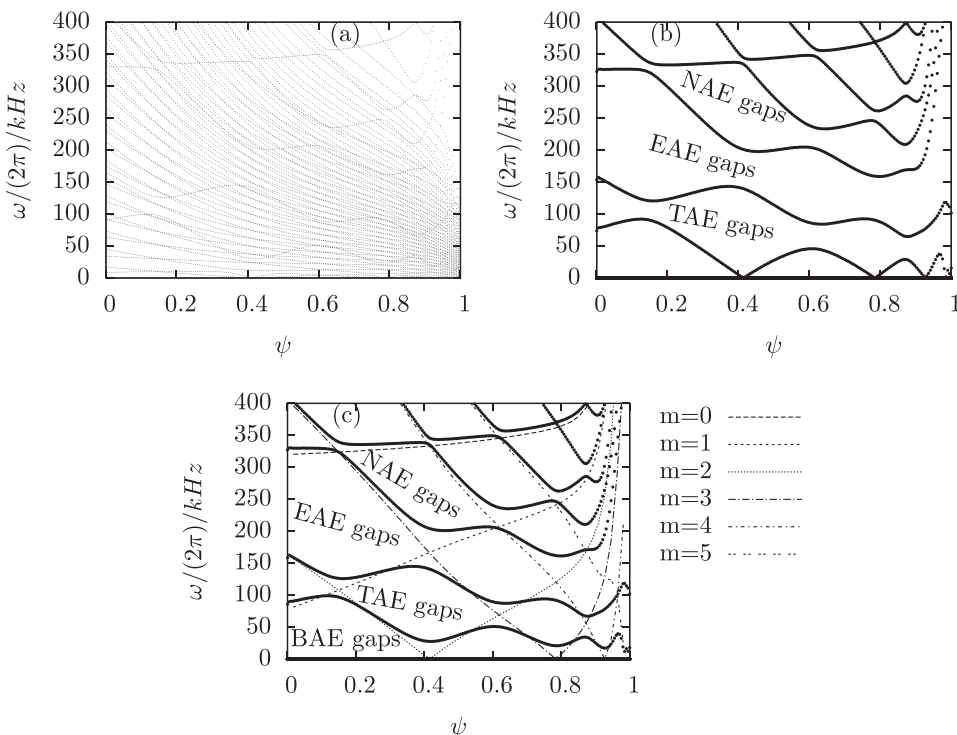


FIG. 7. Full (a), zero β approximation (b), and slow sound approximation (c) of $n = 1$ continua. The poloidal harmonics included in the numerical calculation are in the range $m \in [-20, 40]$. Also plotted on (c) are the $m = 1, 2, 3, 4, 5$ Alfvén continua in the cylindrical limit. The equilibrium used is for EAST discharge #38300 at 3.9 s.

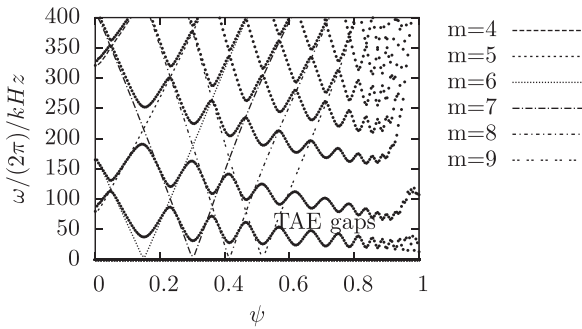


FIG. 8. The slow-sound approximation⁴⁴ of the $n=4$ Alfvén continua for the equilibrium of EAST discharge #38300 at 3.9 s. Also plotted on the figure are the $m=4, 5, 6, 7, 8, 9$ Alfvén continua in the cylindrical limit.

was found. The radial structure of the mode is plotted in Fig. 9(a), which shows that the poloidal harmonics with $m=1$ and $m=2$ are dominant. Figure 9(b) plots the frequency of the mode ($f=103$ kHz) on the graph of the Alfvén continua, which shows that the frequency is within the TAE gap formed due to the coupling of the $m=1$ and $m=2$ harmonics. The mode is thus identified as a TAE mode.

The boundary condition used in obtaining the results in Fig. 9(a) is that the radial plasma displacement ξ_ψ is zero both at the magnetic axis and the LCFS. Examining Fig. 9(a), we can find that the mode structure has singularities at two radial locations $\sqrt{\psi} = 0.74$ and $\sqrt{\psi} = 0.97$. These two locations are also where the frequency of the mode intersects the continua, as is shown in Fig. 9(b). This indicates that the singularities are due to the continuum resonance. These kinds of singularities in the mode structure is typical for realistic equilibria where the Alfvén continua gaps have shear across the radius and thus, a given frequency in a gap usually intersects the continua at some locations. The definition of the Alfvén gap modes requires the frequency of the mode does not intersect the continua. At the location where the frequency intersects the continua, the mode should be locally identified as a singular continuum mode, instead of an Alfvén gap mode. For realistic equilibria, an Alfvén eigenmode found numerically is usually a combination of an Alfvén gap mode and singular continuum modes, as is seen in the case of Fig. 9(a). Analytical theory predicates that the mode structure has a logarithm singularity at the point of

continuum resonance. This kind of singularity can be reproduced by GTAW code (as is shown in Fig. 9(a), the singularity at $\sqrt{\psi} = 0.74$ is of logarithm type). However, the structure near the continuum resonance is sensitive to how the numerical grids are distributed near the point of the continuum resonance (the peak of the logarithm singularity can be easily made lower/higher and wider/narrower by adjusting the radial grids). This kind of singular structure can sometimes blur the mode structure of the gap modes. In numerical calculations, we can avoid the continuum resonance and thus obtain pure gap modes by restricting the radial range to a sub-range near the center of a gap. The boundary condition in this case is set to that ξ_ψ is zero at both the end points of the sub-range. Using this strategy, we recalculate the mode structure and frequency of the TAE in Fig. 9. The results are plotted in Fig. 10, which indicates that the frequency and mode structure in the sub-range are similar to the results given in Fig. 9.

Next, we examine the phase variation of the eigenfunction across the major radius on the midplane. For a up-down symmetric equilibrium, the midplane is special in that it is the mirror plane of the equilibrium. As is mentioned above, for a up-down symmetric equilibrium, the amplitude of the radial displacement of a gap mode can be transformed to a real-valued function. Thus, the phase variation of an eigenmode across the radius on the midplane is zero (or a phase jump of π if eigenfunctions change signs) (note that the location of $\theta=0$ is chosen on the midplane and the amplitude by definition is the value of the perturbation at $\theta=0$). For the up-down asymmetric equilibrium considered here, Figure 10 shows that the real and imaginary parts of the poloidal harmonics have slightly different radial dependence, which indicates that the eigenfunction cannot be exactly transformed to a real function across the radius. This implies that the eigenfunction has phase variation across the radius. The phase of the eigenfunction in Fig. 10 is plotted by the solid line in Fig. 11, which shows that the phase changes across the radius, where the phase is defined relative to the phase at the point very near the left end-point of the computational region. The phase variation in this case is small (only 0.2 rad), which is consistent with the fact that the up-down asymmetry of the equilibrium in Fig. 5 is also small. Since

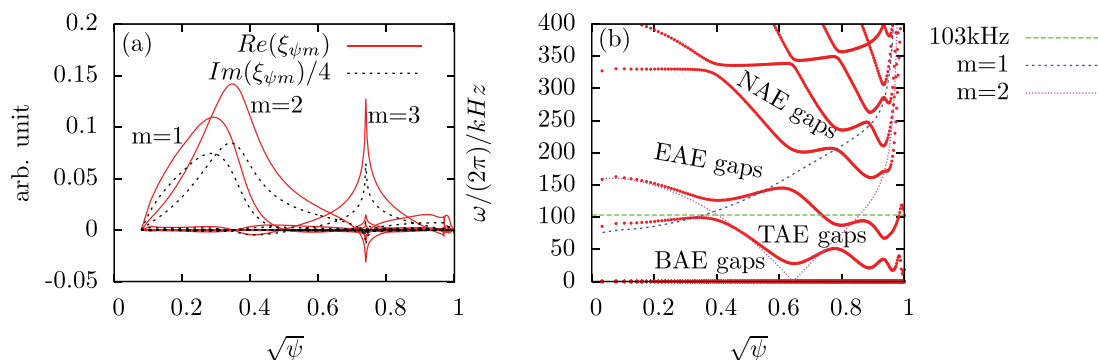


FIG. 9. (a) Amplitude of the poloidal harmonics ($m \in [-3, 8]$) of an $n=1$ TAE as a function of the radial coordinate. (b) The frequency of the TAE mode ($f=103$ kHz) plotted on the Alfvén continua. Also plotted in (b) are the $m=1$ and $m=2$ Alfvén continua in the cylindrical limit. Both the TAE and the Alfvén continua are calculated in the slow sound approximation.^{23,44} The equilibrium is for EAST discharge #38300 at 3.9 s.

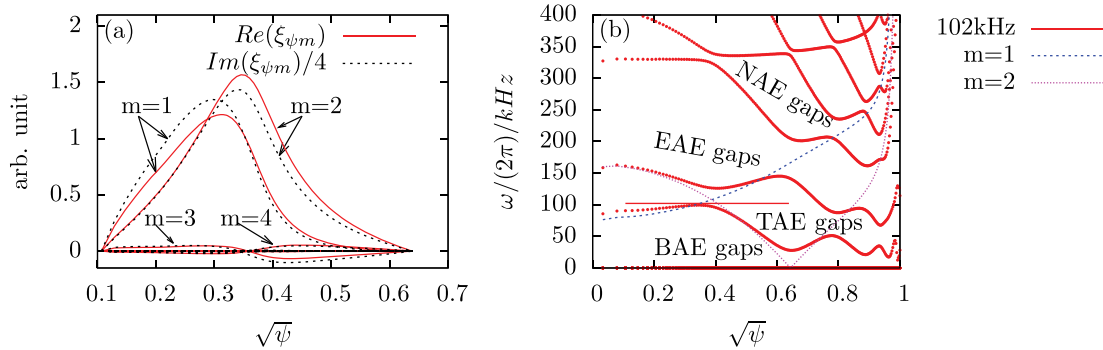


FIG. 10. (a) Amplitude of the poloidal harmonics ($m \in [-8, 18]$) of an $n=1$ TAE (the $m=1$ and $m=2$ harmonics are dominant, with $m=3, m=4$, and all other harmonics being neglectable). (b) The frequency of the TAE ($f=102$ kHz) plotted on the graphic of the Alfvén continua. The radial range of the line of 102 kHz denotes the radial range used in the numerical calculation, which is chosen in order to avoid the continuum resonance. Also plotted on (b) are the $m=1$ and $m=2$ Alfvén continua in the cylindrical limit. The equilibrium is for EAST discharge #38300 at 3.9 s.

the phase variation is small, we need to verify that the small phase variation is due to the up-down asymmetry, instead of numerical errors. In order to achieve this, it is desirable to do a scan in the degree of up-down asymmetry and show that the phase variation relates to the degree of up-down asymmetry. However, for a given equilibrium, there is no method of changing the degree of up-down asymmetry while keeping the equilibrium still an exact one. As a coarse method, we vary the degree of up-down asymmetry artificially by directly varying one of the equilibrium quantities κ_ψ and keeping the others unchanged. The way we modifies κ_ψ is as follows: expand $\kappa_\psi(\psi, \theta)$ in terms of the Fourier series of θ on every flux surface, then multiply the coefficient of the first harmonic $\sin\theta$ by a factor α_1 , and then reconstruct κ_ψ by using the modified Fourier coefficients. Since the term $\sin\theta$ is a up-down asymmetric term, modifying this term will change the degree of up-down asymmetry. The factor α_1 can be considered as a parameter characterizing the degree of up-down asymmetry. Figure 12 plots the original and the modified κ_ψ on one of the flux surfaces, which shows that the degree of up-down asymmetry increases with the increasing of the value of α_1 .

Figure 11 plots the phase variation across the radius for different values of α_1 , which shows that the phase variation increases with the increasing of the value of α_1 , i.e., the phase variation increases with the increasing of the degree of up-down asymmetry.

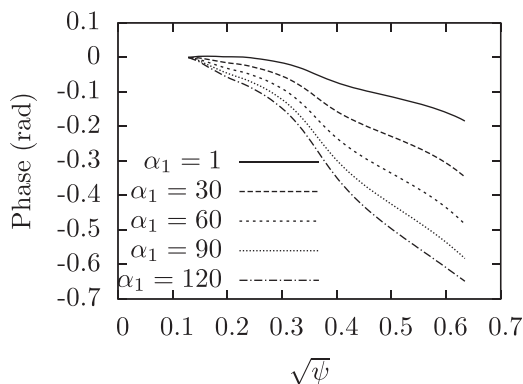


FIG. 11. The phase variations across the radius on the midplane for different values of the degree of up-down asymmetry.

Next, we examine the parity of the TAE in Figure 10. Figure 10(a) shows that the $m=1$ and $m=2$ harmonics interfere constructively at the low-field side of the midplane (note again that the location of $\theta=0$ is on the low field side of the midplane and the amplitudes by definition are the values of the poloidal harmonics at $\theta=0$). This kind of mode structure (i.e., ballooning structure) corresponds to the even TAE (the usual TAE) reported in Refs. 5 and 47, where the frequency of the mode was reported to be near the low continuum tip. As is shown in Fig. 10(b), the frequency of the mode ($f=102$ kHz) is indeed near the low continuum tip (instead of the upper tip) of the gap formed due to the coupling of the $m=1$ and $m=2$ harmonics. By scanning the guess frequency, we attempted to find TAEs with odd parity. However, the results indicate all the TAEs found are of even parity. To explain this, we examine the existence condition of the odd TAEs, which requires that the magnetic shear should be weak and the pressure profile be flat near the radial location of the gap tip. Specifically, the condition is given by⁴⁸

$$\alpha < -s^2 + \varepsilon, \quad (15)$$

where α is the normalized pressure gradient defined by $\alpha = -8\pi R_a q^2 B_a^{-2} dp_0/dr$ with r being the minor radius of flux surfaces,

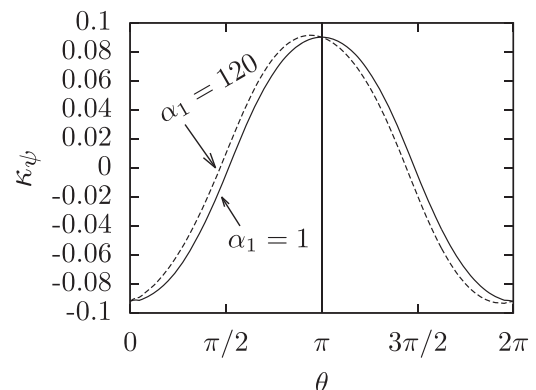


FIG. 12. The original and the modified values of the normal magnetic curvature κ_ψ as a function of the poloidal angle θ on the $\sqrt{\psi} = 0.31$ flux surface. The $\alpha_1 = 1$ case corresponds to the original κ_ψ and the $\alpha_1 = 120$ corresponds to the modified one.

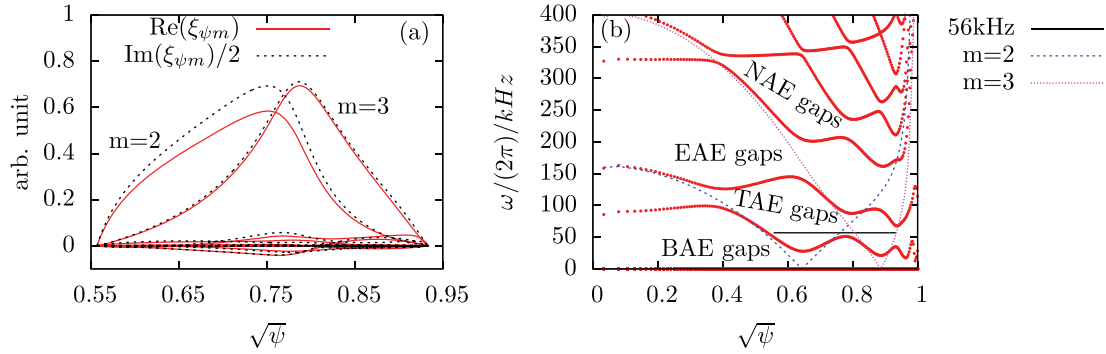


FIG. 13. (a) Amplitude of the poloidal harmonics ($m \in [-8, 18]$) of an $n = 1$ TAE (with the two dominant poloidal harmonics being $m = 2$ and $m = 3$). (b) The frequency of the TAE ($f = 56$ kHz) plotted on the graphic of the Alfvén continua. The radial range of the line of 56 kHz denotes the radial range used in the numerical calculation, which is chosen in order to avoid the continuum resonance. Also plotted on (b) are the $m = 2$ and $m = 3$ Alfvén continua in the cylindrical limit. The equilibrium is for EAST discharge #38300 at 3.9 s.

R_a and B_a being the major radius and strength of the equilibrium magnetic field at the magnetic axis, s is the global magnetic shear defined by $s = rq^{-1}dq/dr$, and ε is the inverse aspect ratio at the location of the mode. For the ($m = 1$, $m = 2$) TAE gap in Fig. 10(b), we have $\alpha = 0.31$, $s = 0.46$, $\varepsilon = 0.08$, and the inequality (15) is invalid, i.e., the existence condition of odd TAEs is not satisfied for this case, which explains why no odd TAEs can be found in the ($m = 1$, $m = 2$) TAE gap.

Next, we investigate the $n = 1$ TAEs in the ($m = 2$, $m = 3$) TAE gap. A TAE with frequency $f = 56$ kHz was found by GTAW. The radial structure of the mode is plotted in Fig. 13(a), which shows the $m = 2$ and $m = 3$ poloidal harmonics are dominant. The TAE found is also of even parity and no odd TAE can be found in this gap. To explain this, we examine again the existence condition (15) for the odd TAEs. For the ($m = 2$, $m = 3$) TAE gap in Fig. 13(b), we have $\alpha = 0.04$, $s = 0.51$, $\varepsilon = 0.18$, and the inequality (15) is invalid, which explains why no odd TAEs can be found.

Figure 14(a) plots the contour of the radial displacement ξ_ψ of the $n = 1$ TAE with frequency $f = 102$ kHz on the poloidal plane, where the poloidal structure with $m = 2$ can be seen. Figure 14(a) shows, as expected, that ξ_ψ on the low-field side is stronger than that of the high field side, i.e., the mode exhibits a ballooning structure. Figure 14 also shows that the TAE is localized in the core region of the plasma. Figure 14(b) plots the contour of the radial

displacement ξ_ψ of the $n = 1$ TAE with frequency $f = 56$ kHz on the poloidal plane, where an $m = 3$ ballooning poloidal structure can be seen. Figure 14 shows that the TAE is localized near the plasma boundary.

The radial displacement obtained from an eigenvalue code is useful in that it relates to the electron number density fluctuation through (the compressible term is neglected)

$$\frac{n_{e1}}{n_{e0}} = -\frac{1}{n_{e0}} \frac{dn_{e0}}{d\Psi} \xi_\psi, \quad (16)$$

where the number density fluctuation n_{e1} can be measured in experiments by microwave reflectometers and beam-emission spectroscopy.^{30,43} This provides a way to compare the results of an eigenvalue code with experimental measurements. The radial displacement also relates approximately to the electron temperature fluctuation through

$$\frac{T_{e1}}{T_{e0}} = -\frac{1}{T_{e0}} \frac{dT_{e0}}{d\Psi} \xi_\psi, \quad (17)$$

where the electron temperature fluctuation T_{e1} can be measured in experiments by electron cyclotron emission radiometers.¹⁸ This provides another way to compare the results of an eigenvalue code with experimental measurements. These kinds of comparisons are planned for the next campaign of experiments on the EAST tokamak.

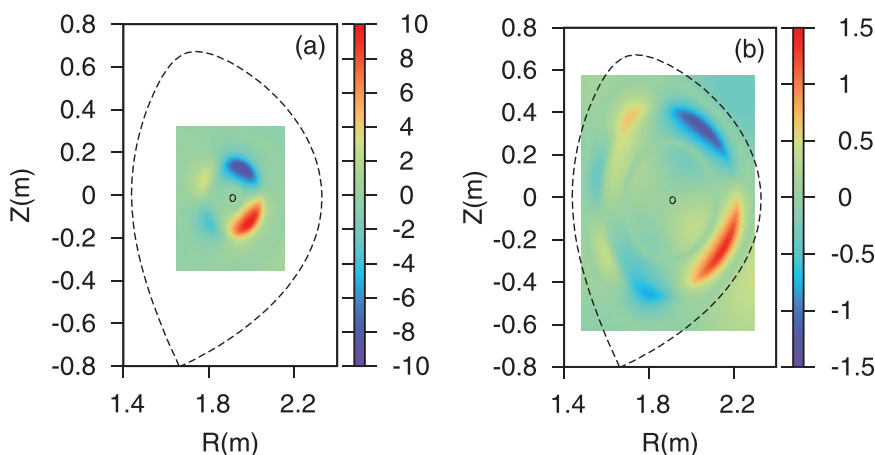


FIG. 14. Contour plot of the radial displacement ξ_ψ of the $f = 102$ kHz (a) and $f = 56$ kHz (b) TAEs on the poloidal plane. The dashed line in the figure indicates the LCFS and the small circle in the center indicates the location of the magnetic axis.

V. SUMMARY

The ideal MHD eigenmodes equations in up-down asymmetric tokamak geometry were solved numerically by the newly built code GTAW. The code was verified with the NOVA code for the Solovév analytical equilibrium and then was used to study Alfvén eigenmodes in the EAST tokamak. The frequency and mode structure of TAEs were calculated. It is numerically demonstrated that up-down asymmetry induces phase variation in the eigenfunction across the radius on the midplane. In addition, we found that TAEs with frequency near the lower tip of the continuum gap exist in the equilibrium considered, whereas TAEs with frequency near the upper tip of the gap do not exist. The results are consistent with the analytical theory for the existence condition of the TAEs.

One feature of the GTAW code is that it can use directly equilibria reconstructed by EFIT from experiments, and thus makes the comparison of the results with experimental observations easy. The further development of the code will be to include consistently plasma rotation, continuum damping, and non-perturbative effects of energetic particles.

ACKNOWLEDGMENTS

The authors would like to thank Dr. G. Y. Fu, Dr. Shaojie Wang, Dr. Y. Todo, Dr. Y. R. Lin-Liu, Dr. N. Xiang, Dr. Deyong Liu, and Dr. Wei Chen for useful discussions. This work was supported by the National Magnetic Confinement Fusion Science Program of China under Grant Nos. 2013GB112010, 2011GB105004, 2011GB101001, and the National Natural Science Foundation of China under Grant No. 11105183.

APPENDIX A: SURFACE OPERATORS IN THE EIGENMODE EQUATIONS

The matrix elements in Eqs. (6) and (7) are spatial differential operators on a flux surface. The expressions of these operators were given in Ref. 34, where the vacuum permeability μ_0 was dropped. Here, for the convenience of reference, we provide the full expression of these operators

$$C_{12} = \omega^2 \rho_0 + \mu_0^{-1} |\nabla \Psi|^2 \mathbf{B}_0 \cdot \nabla \left(\frac{\mathbf{B}_0 \cdot \nabla}{|\nabla \Psi|^2} \right) - (\mu_0^{-1} |\nabla \Psi|^2 S - B_0^2 \sigma) \frac{|\nabla \Psi|^2}{B_0^2} S + 2\kappa_\psi \frac{dp_0}{d\Psi}, \quad (\text{A1})$$

$$C_{21} = 0, \quad (\text{A2})$$

$$C_{22} = -|\nabla \Psi|^2 \nabla \cdot \left(\frac{\nabla \Psi}{|\nabla \Psi|^2} \right), \quad (\text{A3})$$

$$D_{12} = 2\gamma p_0 \kappa_\psi, \quad (\text{A4})$$

$$D_{22} = |\nabla \Psi|^2 + \frac{\gamma p_0 |\nabla \Psi|^2}{\omega^2 \rho_0} \mathbf{B}_0 \cdot \nabla \left(\frac{\mathbf{B}_0 \cdot \nabla}{B_0^2} \right), \quad (\text{A5})$$

$$E_{11} = -\frac{\omega^2 \rho_0 |\nabla \Psi|^2}{B_0^2} - \mu_0^{-1} \mathbf{B}_0 \cdot \nabla \left(\frac{|\nabla \Psi|^2}{B_0^2} \mathbf{B}_0 \cdot \nabla \right), \quad (\text{A6})$$

$$E_{12} = -2\kappa_s \gamma p_0, \quad (\text{A7})$$

$$E_{21} = 2\mu_0^{-1} \kappa_s, \quad (\text{A8})$$

$$E_{22} = \frac{\mu_0^{-1} B_0^2 + \gamma p_0}{B_0^2} + \mu_0^{-1} \frac{\gamma p_0}{\omega^2 \rho_0} \mathbf{B}_0 \cdot \nabla \left(\frac{\mathbf{B}_0 \cdot \nabla}{B_0^2} \right), \quad (\text{A9})$$

$$F_{11} = 2\kappa_s - \left(\frac{\mathbf{B}_0 \times \nabla \Psi}{B_0^2} \right) \cdot \nabla, \quad (\text{A10})$$

$$F_{12} = \sigma \mathbf{B}_0 \cdot \nabla - \mu_0^{-1} \mathbf{B}_0 \cdot \nabla \left(\frac{|\nabla \Psi|^2}{B_0^2} S \right) + 2\kappa_s \frac{dp_0}{d\Psi}, \quad (\text{A11})$$

$$F_{21} = -\frac{1}{B_0^2}, \quad (\text{A12})$$

$$F_{22} = -\mu_0^{-1} \frac{2}{|\nabla \Psi|^2} \kappa_\psi. \quad (\text{A13})$$

APPENDIX B: EXPRESSION OF OPERATORS $\mathbf{B}_0 \cdot \nabla$, $(\mathbf{B}_0 \times \nabla \Psi / B_0^2) \cdot \nabla$, AND $\nabla \Psi \cdot \nabla$ IN FLUX COORDINATES

The eigenmodes Eqs. (6) and (7) were solved numerically in the flux coordinate system (ψ, θ, ζ) , where ψ is a radial coordinate defined by $\psi = (\Psi - \Psi_0) / (\Psi_a - \Psi_0)$ with Ψ_0 and Ψ_b being, respectively, the values of Ψ at the magnetic axis and boundary flux surface, θ is an equal-arc poloidal angle, ζ is a generalized toroidal angle defined by $\zeta \equiv \phi - q(\psi) \delta(\psi, \theta)$ with $\delta(\psi, \theta)$ defined by

$$-\Psi' q \left(\frac{\partial \delta}{\partial \theta} + 1 \right) \frac{R^2}{\mathcal{J}} = g, \quad (\text{B1})$$

where $\Psi' \equiv d\Psi/d\psi = 1/(\Psi_a - \Psi_0)$, $\mathcal{J} = (\nabla \psi \times \nabla \theta \cdot \nabla \zeta)^{-1}$ is the transformation Jacobian of (ψ, θ, ζ) coordinates. The form of \mathcal{J} used in GTAW is given by

$$\mathcal{J} = -\oint \frac{dl_p}{2\pi} \frac{R}{|\nabla \psi|}, \quad (\text{B2})$$

where l_p is the poloidal arc length along magnetic surfaces. The poloidal angle θ determined by this Jacobian is an equal-arc-length poloidal angle. The location $\theta = 0$ is chosen to be on the low field side of the midplane and the positive direction of θ is chosen to be counter clockwise when observers look along the direction of $\nabla \phi$, where the cylindrical coordinate system (R, ϕ, Z) is a right-hand one, with the positive direction of Z pointing vertically up.

In (ψ, θ, ζ) coordinates, the contravariant and covariant form of \mathbf{B}_0 are written, respectively, as

$$\mathbf{B}_0 = -\Psi' [\nabla \zeta \times \nabla \psi + q(\psi) \nabla \psi \times \nabla \theta] \quad (\text{B3})$$

and

$$\mathbf{B}_0 = \left(\Psi' \frac{\mathcal{J}}{R^2} \nabla \psi \cdot \nabla \theta + gq \frac{\partial \delta}{\partial \psi} + g \delta q' \right) \nabla \psi + \left(-\frac{B_0^2}{\Psi'} \mathcal{J} - gq \right) \nabla \theta + g \nabla \zeta. \quad (\text{B4})$$

Using Eqs. (B3) and (B4), the surface operators, $\mathbf{B}_0 \cdot \nabla$ and $(\mathbf{B}_0 \times \nabla \Psi / B_0^2) \cdot \nabla$ in the eigenmode equations are written, respectively, as

$$\mathbf{B}_0 \cdot \nabla = -\Psi' \mathcal{J}^{-1} \left(\frac{\partial}{\partial \theta} + q \frac{\partial}{\partial \zeta} \right), \quad (\text{B5})$$

$$\frac{\mathbf{B}_0 \times \nabla \Psi}{B_0^2} \cdot \nabla = \left(1 + \Psi' g \frac{\mathcal{J}^{-1}}{B_0^2} q \right) \frac{\partial}{\partial \zeta} + \Psi' g \frac{\mathcal{J}^{-1}}{B_0^2} \frac{\partial}{\partial \theta}. \quad (\text{B6})$$

The radial differential operator $\nabla \Psi \cdot \nabla$ in (ψ, θ, ζ) coordinates is written as

$$\nabla \Psi \cdot \nabla = \Psi' |\nabla \psi|^2 \frac{\partial}{\partial \psi} + \Psi' (\nabla \theta \cdot \nabla \psi) \frac{\partial}{\partial \theta} - \Psi' \left[\frac{\partial(q\delta)}{\partial \psi} |\nabla \psi|^2 + q \frac{\partial \delta}{\partial \theta} \nabla \theta \cdot \nabla \psi \right] \frac{\partial}{\partial \zeta}. \quad (\text{B7})$$

APPENDIX C: MAGNETIC CURVATURE AND LOCAL MAGNETIC SHEAR

The eigenmodes Eqs. (6) and (7) involve three important magnetic geometry quantities, namely, the normal magnetic curvature κ_ψ , the geodesic curvature κ_s , and the local magnetic shear S . Next, we give the formulas for calculating these quantities. In the (ψ, θ, ζ) coordinates, the normal curvature is written as

$$\kappa_\psi = -\Psi'^3 R \frac{\mathcal{J}^{-3}}{B_0^2} (R_{\theta\theta} Z_\theta - R_\theta Z_{\theta\theta}) + \frac{\Psi' g^2}{B_0^2} \frac{1}{R^2} \frac{1}{\mathcal{J}} Z_\theta, \quad (\text{C1})$$

and the geodesic curvature is written as

$$\kappa_s = \frac{\mathcal{J}^{-1} g}{B_0^3} \Psi' \frac{\partial B_0}{\partial \theta}, \quad (\text{C2})$$

which indicates that the geodesic curvature is proportional to the poloidal derivative of the magnetic field strength. In Eq. (C1), R_θ , Z_θ , $R_{\theta\theta}$, and $Z_{\theta\theta}$ denote the partial derivatives with respect to the subscripts. The local magnetic shear is written as

$$S = \left[\frac{\partial}{\partial \psi} \left(\frac{g\mathcal{J}}{\Psi' R^2} \right) + \frac{\partial}{\partial \theta} \left(\frac{g\mathcal{J}}{\Psi' R^2} \frac{\nabla \psi \cdot \nabla \theta}{|\nabla \psi|^2} \right) \right] \mathcal{J}^{-1}, \quad (\text{C3})$$

which is related to $dq/d\psi$ through

$$\langle S \rangle = -\frac{2\pi}{\int_0^{2\pi} \mathcal{J} d\theta} \frac{dq}{d\psi}, \quad (\text{C4})$$

where $\langle \dots \rangle$ is the flux surface averaging operator defined by

$$\langle \dots \rangle \equiv \frac{\int_0^{2\pi} (\dots) \mathcal{J} d\theta}{\int_0^{2\pi} \mathcal{J} d\theta}. \quad (\text{C5})$$

Equation (C4) can be used to verify that the numerical implementation of S is correct. The local magnetic shear can also be calculated in the cylindrical coordinate system, which gives

$$S = \frac{1}{\Psi_R^2 + \Psi_Z^2} \frac{1}{R^2} \left(g \Psi_{ZZ} + g' \Psi_Z^2 + g \Psi_{RR} + \Psi_R \frac{g' \Psi_{RR} - g}{R} \right) - \frac{1}{[\Psi_R^2 + \Psi_Z^2]^2} \frac{g}{R^2} (4 \Psi_R \Psi_{RZ} \Psi_Z + 2 \Psi_Z^2 \Psi_{ZZ} + 2 \Psi_R^2 \Psi_{RR}), \quad (\text{C6})$$

where Ψ_R , Ψ_Z , Ψ_{RR} , Ψ_{ZZ} , Ψ_{RZ} denote the partial derivatives with respect to the subscripts. In addition, the parallel current term $\sigma \equiv \mathbf{B}_0 \cdot \mathbf{J}_0 / B_0^2$ is written as

$$\sigma = g \frac{dp_0}{d\Psi} \frac{1}{B_0^2} + \frac{1}{\mu_0} \frac{dg}{d\Psi}. \quad (\text{C7})$$

The radial profiles of κ_ψ , κ_s , S , and $\mu_0 \sigma$ for EAST discharge #38300 at 3.9 s are plotted in Fig. 15.

APPENDIX D: NUMERICAL METHODS IN GTAW CODE

Since we consider perturbation with a single toroidal number n , the differential with respect to the toroidal angle ζ can be treated analytically. The differential with respect to θ is treated by using the Fourier spectrum expansion method. After taking the inner product over θ and using Eq. (7) in Eq. (6) to eliminate the poloidal harmonics of ζ_s and $\nabla \cdot \xi$ in favor of those of P_1 and ξ_ψ , we obtain the following system of ordinary differential equations for the poloidal harmonics of P_1 and ξ_ψ :

$$\frac{d}{d\psi} \begin{pmatrix} P_1^{(1)}(\psi) \\ \vdots \\ P_1^{(L)}(\psi) \\ \xi_\psi^{(1)}(\psi) \\ \vdots \\ \xi_\psi^{(L)}(\psi) \end{pmatrix} = \mathbb{A} \begin{pmatrix} P_1^{(1)}(\psi) \\ \vdots \\ P_1^{(L)}(\psi) \\ \xi_\psi^{(1)}(\psi) \\ \vdots \\ \xi_\psi^{(L)}(\psi) \end{pmatrix}, \quad (\text{D1})$$

where L is the total number of the poloidal harmonics included in the Fourier expansion, \mathbb{A} is a $2L \times 2L$ matrix with the matrix elements being functions of ψ and ω^2 , $P_1^{(j)}$ and $\xi_\psi^{(j)}$ with $j=1, 2, \dots, L$ are the amplitudes of the poloidal harmonics of P_1 and ξ_ψ , respectively ($\xi_\psi^{(j)}$ is different from $\xi_{\psi j}$ defined in Eq. (12); the relation between them is $\xi_\psi^{(j)} = \xi_{\psi(j+l-1)}$ with l being the smallest harmonics number (can be negative) included in the Fourier expansion).

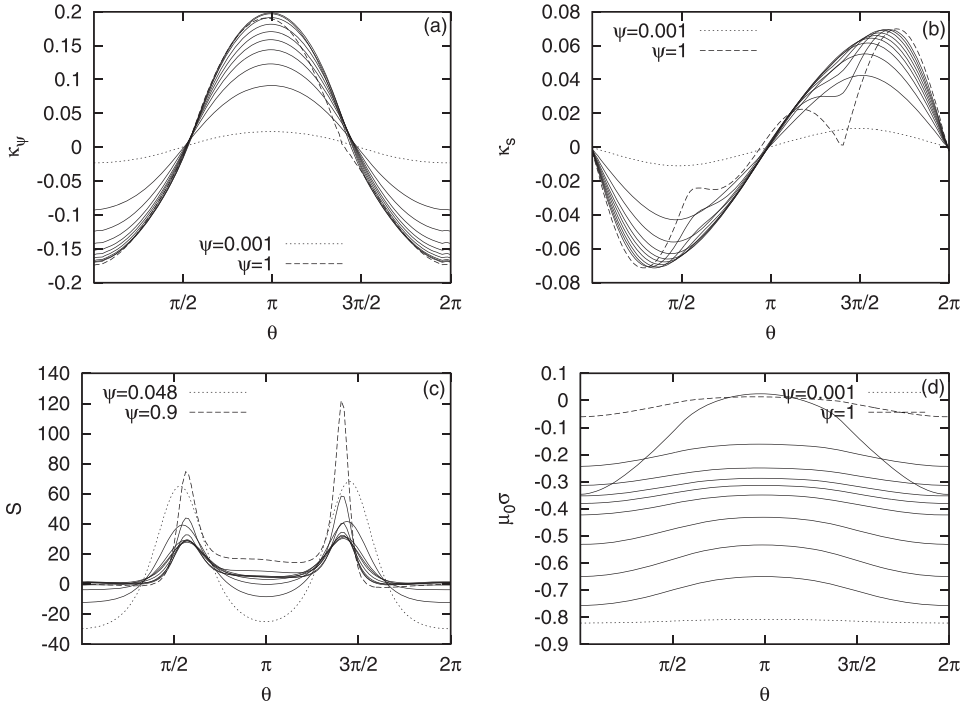


FIG. 15. The normal magnetic curvature (a), geodesic magnetic curvature (b), local magnetic shear (c), and parallel current (d) as a function of the poloidal angle for EAST discharge #38300 at 3.9 s. All dimensional quantities are in SI units. Different lines in the figure correspond to values of the quantities on different magnetic surfaces.

We use fixed boundary conditions for the radial plasma displacement ξ_ψ , i.e., ξ_ψ is set to be zero at both the ending points of the radial computational region. Given the values of all the poloidal harmonics of P_1 and ξ_ψ at the left endpoint, Eq. (D1) can be integrated by the first-order Euler scheme from the left endpoint to the right one. Note that we are solving a two-points boundary problem for which the values of the poloidal harmonics of P_1 are unknown at the left endpoint. Further note that we are solving an eigenvalue problem for which there is an additional equation for ω^2

$$\frac{d\omega^2}{d\psi} = 0. \quad (\text{D2})$$

Noting these, it is natural to use the shooting method to solve the eigenvalue problem in Eq. (D1). The shooting process finally reduces to finding the root of a system of multivariable nonlinear equations $F(\mathbf{X}) = 0$. In our case, \mathbf{X} and $F(\mathbf{X})$ are given by

$$\mathbf{X} = \begin{pmatrix} P_1^{(1)}(\psi_a) \\ P_2^{(2)}(\psi_a) \\ \vdots \\ P_1^{(L-1)}(\psi_a) \\ \omega^2(\psi_a) \end{pmatrix}, \quad F(\mathbf{X}) = \begin{pmatrix} \xi_\psi^{(1)}(\psi_b) \\ \xi_\psi^{(2)}(\psi_b) \\ \vdots \\ \xi_\psi^{(L-1)}(\psi_b) \\ \xi_\psi^{(L)}(\psi_b) \end{pmatrix}, \quad (\text{D3})$$

where ψ_a and ψ_b are the two end-points. The value of the last poloidal harmonic of P_1 at the left end-point, i.e., $P_1^{(L)}(\psi_a)$, is set to be a small nonzero constant during the shooting process. Once a root is obtained for $F(\mathbf{X}) = 0$, the last component of \mathbf{X} gives the eigenfrequency and the eigenfunctions can be obtained by integrating Eq. (D1) with this eigenfrequency.

- ¹G. Y. Fu and J. W. Van Dam, *Phys. Fluids B* **1**, 1949 (1989).
- ²R. Nazikian, G. Y. Fu, Z. Chang, S. H. Batha, H. Berk, R. V. Budny, Y. Chen, C. Z. Cheng, D. S. Darrow, N. N. Gorelenkov, F. M. Levinton, S. Medley, M. P. Petrov, M. Redi, E. Ruskov, D. A. Spong, R. B. White, and S. J. Zweben, *Phys. Plasmas* **5**, 1703 (1998).
- ³R. Nazikian, N. N. Gorelenkov, B. Alper, H. L. Berk, D. Borba, R. V. Budny, G. Y. Fu, W. W. Heidbrink, G. J. Kramer, M. A. Makowski, S. D. Pinches, S. E. Sharapov, W. M. Solomon, E. J. Strait, R. B. White, M. A. Van Zeeland, and JET-EFDA contributors, *Phys. Plasmas* **15**, 056107 (2008).
- ⁴Y. Todo and T. Sato, *Phys. Plasmas* **5**, 1321 (1998).
- ⁵G. Y. Fu, C. Z. Cheng, R. Budny, Z. Chang, D. S. Darrow, E. Fredrickson, E. Mazzucato, R. Nazikian, K. L. Wong, and S. Zweben, *Phys. Plasmas* **3**, 4036 (1996).
- ⁶K.-L. Wong, *Plasma Phys. Controlled Fusion* **41**, R1 (1999).
- ⁷B. N. Breizman and S. E. Sharapov, *Plasma Phys. Controlled Fusion* **53**, 054001 (2011).
- ⁸M. A. Van Zeeland, W. W. Heidbrink, R. K. Fisher, M. García Muñoz, G. J. Kramer, D. C. Pace, R. B. White, S. Aekaslopolo, M. E. Austin, J. E. Boom, I. G. J. Classen, S. da Graça, B. Geiger, M. Gorelenkova, N. N. Gorelenkov, A. W. Hyatt, N. Luhmann, M. Maraschek, G. R. McKee, R. A. Moyer, C. M. Muscatello, R. Nazikian, H. Park, S. Sharapov, W. Suttrop, G. Tardini, B. J. Tobias, Y. B. Zhu, and DIII-D and ASDEX Upgrade Teams, *Phys. Plasmas* **18**, 056114 (2011).
- ⁹M. V. Zeeland, N. Gorelenkov, W. Heidbrink, G. Kramer, D. Spong, M. Austin, R. Fisher, M. G. Munoz, M. Gorelenkova, N. Luhmann, M. Murakami, R. Nazikian, D. Pace, J. Park, B. Tobias, and R. White, *Nucl. Fusion* **52**, 094023 (2012).
- ¹⁰W. W. Heidbrink, N. N. Gorelenkov, Y. Luo, M. A. Van Zeeland, R. B. White, M. E. Austin, K. H. Burrell, G. J. Kramer, M. A. Makowski, G. R. McKee, and R. Nazikian, *Phys. Rev. Lett.* **99**, 245002 (2007).
- ¹¹Y. Todo, H. L. Berk, and B. N. Breizman, *Phys. Plasmas* **10**, 2888 (2003).
- ¹²R. B. White, E. Fredrickson, D. Darrow, M. Zarnstorff, R. Wilson, S. Zweben, K. Hill, Y. Chen, and G. Fu, *Phys. Plasmas* **2**, 2871 (1995).
- ¹³C. Z. Cheng, L. Chen, and M. S. Chance, *Ann. Phys. (NY)* **161**, 21 (1984).
- ¹⁴W. W. Heidbrink, *Phys. Plasmas* **15**, 055501 (2008).
- ¹⁵N. N. Gorelenkov, *Phys. Rev. Lett.* **95**, 265003 (2005).
- ¹⁶L. Yu, G.-Y. Fu, and Z.-M. Sheng, *Phys. Plasmas* **16**, 072505 (2009).
- ¹⁷G. Y. Fu and H. L. Berk, *Phys. Plasmas* **13**, 052502 (2006).
- ¹⁸B. J. Tobias, I. G. J. Classen, C. W. Domier, W. W. Heidbrink, N. C. Luhmann, R. Nazikian, H. K. Park, D. A. Spong, and M. A. Van Zeeland, *Phys. Rev. Lett.* **106**, 075003 (2011).
- ¹⁹W. Chen, X. T. Ding, Q. W. Yang, Y. Liu, X. Q. Ji, Y. P. Zhang, J. Zhou, G. L. Yuan, H. J. Sun, W. Li, Y. Zhou, Y. Huang, J. Q. Dong, B. B. Feng, X. M. Song, Z. B. Shi, Z. T. Liu, X. Y. Song, L. C. Li, X. R. Duan, and Y. Liu, *Phys. Rev. Lett.* **105**, 185004 (2010).

- ²⁰M. Xu, W. Chen, L. Q. Hu, R. J. Zhou, G. Q. Zhong, T. H. Shi, L. Q. Xu, Y. Zhang, Y. W. Sun, S. Y. Lin, B. Shen, and EAST Team, *Plasma Phys. Controlled Fusion* **55**, 065002 (2013).
- ²¹B. Wan, J. Li, H. Guo, Y. Liang, G. Xu, and X. Gong for the EAST Team and International Collaborators, *Nucl. Fusion* **53**, 104006 (2013).
- ²²P. Lauber, S. Gunter, A. Konies, and S. Pinches, *J. Comput. Phys.* **226**, 447 (2007).
- ²³W. Deng, Z. Lin, I. Holod, Z. Wang, Y. Xiao, and H. Zhang, *Nucl. Fusion* **52**, 043006 (2012).
- ²⁴J. Lang, Y. Chen, S. E. Parker, and G.-Y. Fu, *Phys. Plasmas* **16**, 102101 (2009).
- ²⁵Y. Chen, S. E. Parker, J. Lang, and G.-Y. Fu, *Phys. Plasmas* **17**, 102504 (2010).
- ²⁶Ph. Lauber, S. Günter, and S. D. Pinches, *Phys. Plasmas* **12**, 122501 (2005).
- ²⁷R. R. Mett and S. M. Mahajan, *Phys. Fluids B* **4**, 2885 (1992).
- ²⁸H. S. Zhang, Z. Lin, I. Holod, X. Wang, Y. Xiao, and W. L. Zhang, *Phys. Plasmas* **17**, 112505 (2010).
- ²⁹N. N. Gorelenkov, H. L. Berk, N. A. Crocker, E. D. Fredrickson, S. Kaye, S. Kubota, H. Park, W. Peebles, S. A. Sabbagh, S. E. Sharapov, D. Stutmat, K. Tritz, F. M. Levinton, H. Yuh, NSTX Team, and JET EFDA Contributors, *Plasma Phys. Controlled Fusion* **49**, B371 (2007).
- ³⁰M. A. Van Zeeland, G. J. Kramer, M. E. Austin, R. L. Boivin, W. W. Heidbrink, M. A. Makowski, G. R. McKee, R. Nazikian, W. M. Solomon, and G. Wang, *Phys. Rev. Lett.* **97**, 135001 (2006).
- ³¹G. Y. Fu, *Phys. Plasmas* **2**, 1029 (1995).
- ³²S. E. Sharapov, B. Alper, H. L. Berk, D. N. Borba, B. N. Breizman, C. D. Challis, A. Fasoli, N. C. Hawkes, T. C. Hender, J. Mailloux, S. D. Pinches, D. Testa, and EFDA JET work programme, *Phys. Plasmas* **9**, 2027 (2002).
- ³³B. N. Breizman, H. L. Berk, M. S. Pekker, S. D. Pinches, and S. E. Sharapov, *Phys. Plasmas* **10**, 3649 (2003).
- ³⁴C. Cheng and M. Chance, *J. Comput. Phys.* **71**, 124 (1987).
- ³⁵N. N. Gorelenkov, C. Z. Cheng, and W. M. Tang, *Phys. Plasmas* **5**, 3389 (1998).
- ³⁶L.-J. Zheng and M. Kotschenreuther, *J. Comput. Phys.* **211**, 748 (2006).
- ³⁷L. Zheng, M. Kotschenreuther, and J. V. Dam, *J. Comput. Phys.* **229**, 3605 (2010).
- ³⁸D. Borba and W. Kerner, *J. Comput. Phys.* **153**, 101 (1999).
- ³⁹D. Spong, *Nucl. Fusion* **53**, 053008 (2013).
- ⁴⁰C. Z. Cheng, *Phys. Rep.* **211**, 1 (1992).
- ⁴¹N. N. Gorelenkov, C. Z. Cheng, and G. Y. Fu, *Phys. Plasmas* **6**, 2802 (1999).
- ⁴²B. Tobias, E. Bass, I. Classen, C. Domier, B. Grierson, W. Heidbrink, N. Luhmann Jr, R. Nazikian, H. Park, D. Spong, and M. V. Zeeland, *Nucl. Fusion* **52**, 103009 (2012).
- ⁴³W. W. Heidbrink, M. E. Austin, D. A. Spong, B. J. Tobias, and M. A. Van Zeeland, *Phys. Plasmas* **20**, 082504 (2013).
- ⁴⁴M. S. Chu, J. M. Greene, L. L. Lao, A. D. Turnbull, and M. S. Chance, *Phys. Fluids B* **4**, 3713 (1992).
- ⁴⁵L. Lao, H. S. John, R. Stambaugh, A. Kellman, and W. Pfeiffer, *Nucl. Fusion* **25**, 1611 (1985).
- ⁴⁶G. Q. Li, Q. L. Ren, J. P. Qian, L. L. Lao, S. Y. Ding, Y. J. Chen, Z. X. Liu, B. Lu, and Q. Zang, *Plasma Phys. Controlled Fusion* **55**, 125008 (2013).
- ⁴⁷G. J. Kramer, S. E. Sharapov, R. Nazikian, N. N. Gorelenkov, and R. V. Budny, *Phys. Rev. Lett.* **92**, 015001 (2004).
- ⁴⁸H. L. Berk, J. W. Van Dam, D. Borba, J. Candy, G. T. A. Huysmans, and S. Sharapov, *Phys. Plasmas* **2**, 3401 (1995).